18. R. N. Clark, G. A. Swayze, A. Gallagher, T. V. V. King, W. M. Calvin, "The U.S. Geological Survey Digital Spectral Library: Version 1: 0.2 to 3.0 μm," U.S. Geological Survey Open File Report 93-592.
19. O. Bain and P. A. Giguere, *Can. J. Chem.* **33**, 527 (1955); R. L. Miller and D. F. Hornig, *J. Chem. Phys.* **34**, 265 (1961).
20. P. A. Giguere and K. B. Harvey, *J. Mol. Spectrosc.* **3**, 36 (1959).
21. We measured IR diffuse-reflectance spectra for frozen (~80 K) aqueous solutions of H_2O_2 at concentrations of 0, 0.5, 1, and 1.5%. The solution contained spectrally neutral diamond powder, producing a matte surface without specular reflection. Ice grain sizes were 5 to 15 μm. The factor relating concentration and relative band depth was found after correcting for the minor dependence of relative band depth on grain size, determined from radiative-transfer calculations (*25*). Grain sizes were estimated by comparing measured and computed IR reflectivities. The fractional standard error for the derived factor is 15%. We assume that the band depth is invariant with temperature; the behavior of ice bands [W. M. Grundy and B. Schmitt, *J. Geophys. Res.* **103**. 25809 (1998)] indicates that errors of ±20% are possible. Considering other error sources, the uncertainty in the derived H_2O_2 abundance is estimated to be ±50.
22. P. A. Gerakines, W. A. Schutte, P. Ehrenfreund, *Astron. Astrophys.* **312**, 289 (1996).
23. We adopt, for the effective penetration depth, that level for which the optical depth for equivalent isotropic scatterers is unity. Using similarity relations [B. Hapke, *Theory of Reflectance and Emittance Spectroscopy* (Cambridge Univ. Press, Cambridge, 1993), p. 197] with computed single-scattering albedos and asymmetry parameters (*25*), we find penetration depths for a nonporous medium of 60-μm ice grains of about 60, 250, and 500 μm for wavelengths of 3.5 μm, 210 nm, and 300 nm, respectively.
24. The reflectance factor is the ratio of the observed radiance to that of a perfectly diffuse plane reflector illuminated at the same geometry [B. Hapke (*23*), p. 262].
25. R. W. Carlson and T. Arakelian [*Antarctic J. U. S.* **28**, 256 (1993)] outline the computational method. We used UV and IR optical constants from S. G. Warren [*Appl. Opt.* **23**, 1206 (1984)] and J. E. Bertie, H. J. Labbé, and E. Whalley [*J. Chem. Phys.* **50**, 4501 (1969)], respectively.
26. C. L. Lin, N. K. Rohatgi, W. B. DeMore, *Geophys. Res. Lett.* **5**, 113 (1978).
27. A. R. Hendrix, C. A. Barth, C. W. Hord, A. L. Lane, *Icarus* **135**, 79 (1998).
28. Samples 3 mm thick were frozen, forming granular, diffusing surfaces. The diffuse reflectance was measured, avoiding specular reflection. The UV and IR laboratory measurements were performed at the JPL Vibrational Spectroscopy Laboratory with the use of an Analect diffuse-reflectance attachment with Bio-Rad FTS 6000 and Cary 5E spectrometers.
29. The 3.4 × 10^{-4} M data from (*26*) were used.
30. M. T. Sieger, W. C. Simpson, T. M. Orlando, *Nature* **394**, 554 (1998).
31. We used electron and ion fluxes (for an unmagnetized body at Europa's orbit) and stopping depths in ice from J. F. Cooper, R. E. Johnson, B. H. Mauk, and N. Gehrels (*Icarus*, in preparation). Ion fluxes were increased by a factor of 2 for the finite gyroradius effect (*4*).
32. M. Cottin and M. Lefort, *J. Chim. Phys.* **52**, 545 (1955). Measurements for other particles are needed.
33. W. F. Huebner, J. J. Keady, S. P. Lyon, *Astrophys. Space Sci.* **195**, 1 (1992).
34. J. A. Ghormley and A. C. Stewart, *J. Am. Chem. Soc.* **78**, 2934 (1956).
35. R. Schriever, M. Chergui, N. Schwentner, *J. Phys. Chem.* **95**, 6124 (1991).
36. D. T. Hall, D. F. Strobel, P. D. Feldman, M. A. McGrath, H. A. Weaver, *Nature* **373**, 677 (1995).
37. D. L. Domingue and A. L. Lane, *Geophys. Res. Lett.* **25**, 4421 (1998).
38. Portions of the work described herein were performed at the Jet Propulsion Laboratory, California Institute of Technology, under contract to the National Aeronautics and Space Administration.

11 January 1999; accepted 22 February 1999

Arctic Ozone Loss Due to Denitrification

A. E. Waibel,[1]* Th. Peter,[1]† K. S. Carslaw,[1]‡ H. Oelhaf,[2]
G. Wetzel,[2] P. J. Crutzen,[1] U. Pöschl,[1]§ A. Tsias,[1] E. Reimer,[3]
H. Fischer[1]

Measurements from the winter of 1994–95 indicating removal of total reactive nitrogen from the Arctic stratosphere by particle sedimentation were used to constrain a microphysical model. The model suggests that denitrification is caused predominantly by nitric acid trihydrate particles in small number densities. The denitrification is shown to increase Arctic ozone loss substantially. Sensitivity studies indicate that the Arctic stratosphere is currently at a threshold of denitrification. This implies that future stratospheric cooling, induced by an increase in the anthropogenic carbon dioxide burden, is likely to enhance denitrification and to delay until late in the next century the return of Arctic stratospheric ozone to preindustrial values.

As a result of international regulations, tropospheric chlorofluorocarbon (CFC) concentrations have started to decline (*1*) and stratospheric concentrations are expected to follow with a time delay of 3 to 5 years (*2*). It is therefore expected that the severe chlorine-catalyzed ozone losses that have occurred over the Antarctic and more recently also over the Arctic (*3, 4*) will gradually disappear, although this process may take several decades.

Recent Arctic ozone losses have been associated with particularly low temperatures, as in the winters 1992–93, 1994–95, 1995–96, and 1996–97 (*5*). Reduction of odd nitrogen (NO_x = NO + NO_2) concentrations in the gas phase is an important factor in determining the severity of ozone destruction (*6*). This NO_x reduction may be either temporary via conversion of NO_x into HNO_3 catalyzed by aerosol surfaces (denoxification), or permanent via removal of HNO_3 by sedimenting

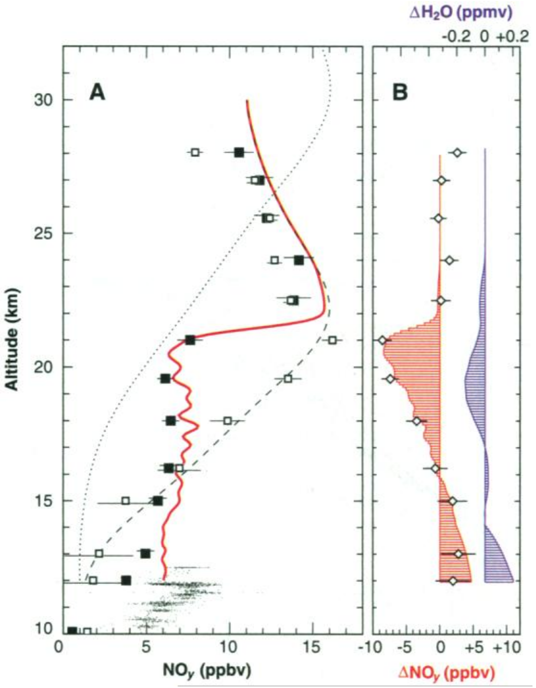

Fig. 1. (**A**) Arctic NO_y profiles in mid-February 1995. Symbols: squares, balloon-borne MIPAS-B observations (*12*); dots, aircraft-borne observations (*16*). Solid symbols are NO_y measurements; open symbols mark NO_y^* deduced from MIPAS N_2O measurements (*13*). NO_y^* represents the unperturbed case (without denitrification). The model calculations are denoted by lines [dotted line, mid-latitude reference NO_y profile (*28*); dashed line, scenario 0 with subsidence of air only (no particle sedimentation); red line, scenario 3 showing the effect of denitrification due to sedimenting ice and NAT particles]. (**B**) Vertical redistribution of NO_y (red) and H_2O (blue). In addition, measured ΔNO_y is shown (◇).

---

[1] Max-Planck-Institut für Chemie, Post Office Box 3060, 55020 Mainz, Germany. [2] Forschungszentrum Karlsruhe, Institut für Meteorologie und Klimaforschung, Post Office Box 3640, D-76021 Karlsruhe, Germany. [3] FU Berlin, Institut für Meteorologie, Carl-Heinrich-Becker-Weg 6-10, D-12165 Berlin, Germany.

*Present address: Lufthansa Systems, FRA4E/DCS, Hugo-Eckner-Ring, D-60549 Frankfurt, Germany.

†To whom correspondence should be addressed. Present address: Institute for Atmospheric Sciences, ETH Zürich, HPP Hönggerberg, CH-8093 Zürich, Switzerland. E-mail: thomas.peter@atmos.umnw.ethz.ch

‡Present address: Environment Centre, University of Leeds, Leeds LS2 9JT, UK.

§Present address: Institut für Wasserchemie, TU München, Marchioninistraβe 17, D-81377 München, Germany.

polar stratospheric cloud (PSC) particles (denitrification). Recent modeling studies (*7*) have indicated that the denitrification that occurs in the Antarctic may not be essential to explain severe ozone loss because Antarctic temperatures remain sufficiently low to allow for continuous denoxification and activation of chlorine via heterogeneous reactions on PSCs. In the Arctic, where temperatures are higher than in the Antarctic, denitrification plays a more important role and can lead to increased ozone loss over the course of the winter (*8*).

Despite future decreases in chlorine, lower stratospheric temperatures resulting from anthropogenic greenhouse forcing might intensify ozone destruction by (i) enhancing heterogeneous chlorine activation rates, (ii) increasing the frequency of occurrence of PSCs, or (iii) intensifying denitrification. Using a general circulation model with simplified stratospheric chemistry including processes (i) and (ii) but not (iii), Shindell *et al.* (*9*) calculated that maximum ozone losses in the Arctic are expected around 2015, because of an 8 to 10 K colder Arctic spring stratosphere resulting from positive feedbacks between radiative, dynamical, and chemical influences. Other studies have shown less cooling of the Arctic lower stratosphere (*10*) or even an enhanced frequency of stratospheric warmings (*11*).

Here, we concentrate on a refined modeling of nitric acid redistribution by particle sedimentation, and show that denitrification in the Arctic winter 1994–95 accounted for up to 35% of the total ozone loss in the middle of the ozone layer.

Balloon-borne measurements of total reactive nitrogen, NO_y (= NO_x + HNO_3 + $ClONO_2$ + $2N_2O_5$ + HO_2NO_2), recorded by the MIPAS-B instrument (*12*) in the Arctic vortex on 11 February 1995 indicate a 50% deficit of NO_y between 16 and 22 km (Fig. 1A). This is clearly identified by the difference between measured NO_y and NO_y^* (Fig. 1B) [NO_y^* is the value of NO_y assuming no denitrification, denoxification, or mixing of nonvortex air into the vortex (*13*), and was derived from simultaneous N_2O measurements].

Denoxification can be excluded from the balloon-borne temperature measurements with values above 200 K. Following the procedure described by Michelsen *et al.* (*14*), we used MIPAS-B CH_4 and N_2O measurements to differentiate between the NO_y lost as a result of mixing and that lost by sedimenting particles, and found that at least 82% of the observed deficit was due to vertical redistribution of NO_y by sedimenting particles (*15*). This is corroborated by a particularly strong surplus of total reactive nitrogen below 14 km altitude due to evaporating particles. This nitrification of the lowermost stratosphere was also observed on 9, 18, 21, and 24 February aboard a research aircraft carrying two instruments measuring NO_y and HNO_3 (*16*). A second balloon flight 10 hours before MIPAS from the same location (*17*) showed the same signature of vertical redistribution, revealing that air masses separated by as much as 1500 km had been denitrified. These measurements confirm other indications of Arctic denitrification (*18*).

These observations can be explained only in terms of HNO_3 particle sedimentation, leading to denitrification at high altitudes and to nitrification below. A consideration of fall velocities as a function of particle radius shows that HNO_3 must be incorporated into large particles in order to fall far enough during the Arctic winter. Nitric acid–containing liquid aerosols (*19*) have typical radii between 0.01 and 0.4 μm, which constrains their sedimentation speed to less than a few meters per day (*20*). Likewise, if all background particles served as sites for growth of solid nitric acid trihydrate (NAT ≡ $HNO_3 \cdot 3H_2O$), these NAT particles would re-

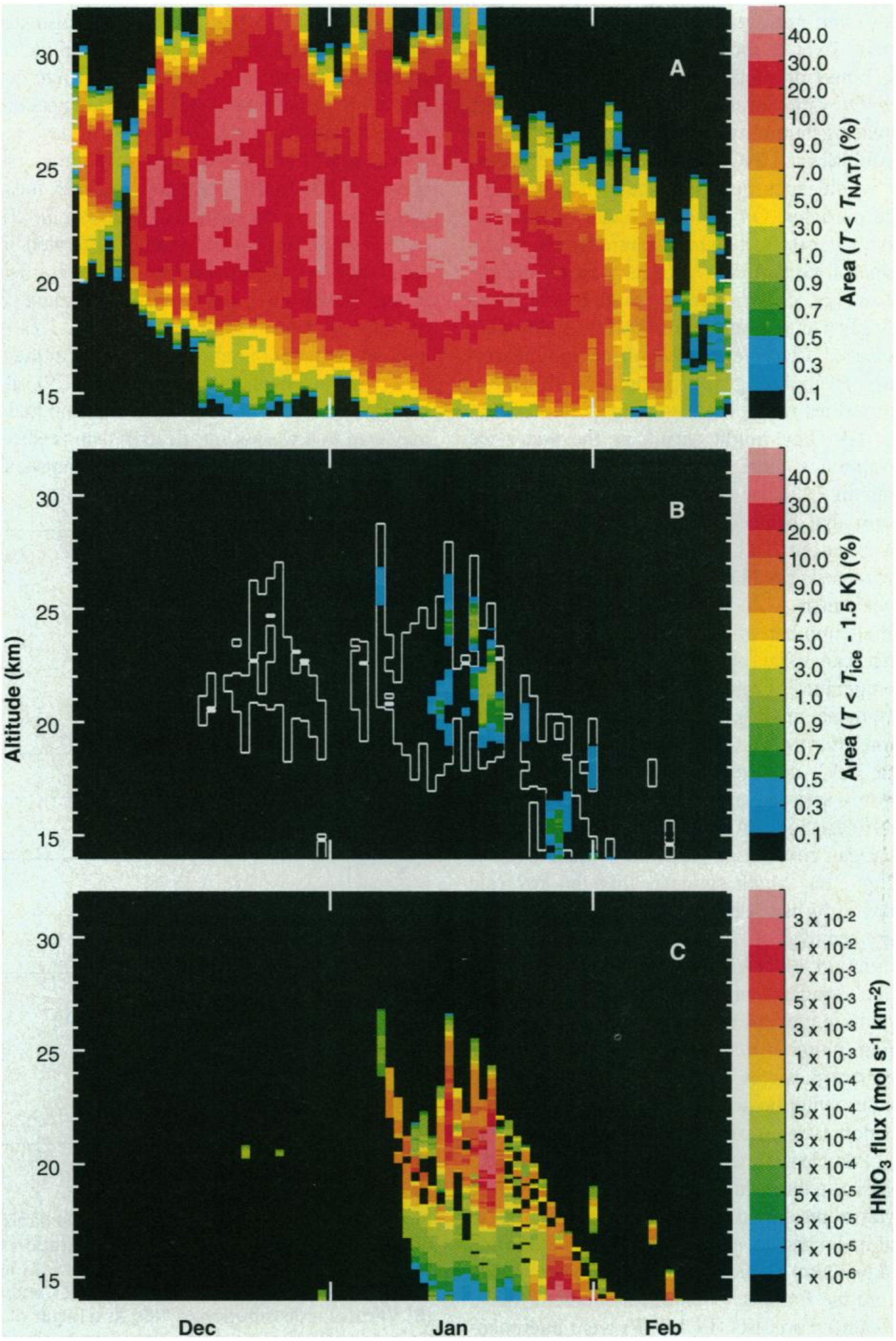

Fig. 2. (**A**) Fraction of vortex area where $T < T_{NAT}$. (**B**) Fraction of vortex area where $T < T_{ice} - 1.5$ K (colored) and where $T < T_{ice}$ (enclosed by white line). (**C**) Vortex-averaged downward HNO_3 flux due to sedimenting particles (scenario 3).

main too small to promote denitrification (*21*).

In contrast, ice particles can grow to the large sizes necessary for rapid gravitational settling and have a high potential to denitrify stratospheric air because they strongly incorporate gaseous HNO_3 in the form of NAT during their growth (*22*). In situ observations suggest the existence of a highly selective ice activation mechanism in synoptic-scale ice clouds, leading to number densities in the range $n_{ice} = 10^{-3}$ to 10^{-2} cm^{-3} (*23*). Such ice particles rapidly attain radii of several micrometers (with fall velocities up to 1 km per day) and remove HNO_3 from their environment. Even if most HNO_3 originally resided in liquid droplets (*19*), their relatively high HNO_3 vapor pressure (enhanced by the decreasing humidity as a result of ice growth) would force HNO_3 into the gas phase, where it would subsequently cocondense onto the ice particles. On the other hand, in the relatively warm Arctic stratosphere the short lifetime of ice particles restricts their efficiency. However, denitrification could be enhanced if only a small number of NAT particles were released after evaporation of ice upon warming. Evaporating ice particles with HNO_3 impurities might undergo one of two changes: (i) They might shrink as the water ice evaporates until large pure NAT residuals remain (*22*); or (ii) a NAT coating might form that protects the ice against complete evaporation (*24*), although recent laboratory work casts doubt on the existence of the latter mechanism (*22*). In both cases, the result is a small number of HNO_3-containing particles that can exist up to the NAT equilibrium temperature, typically ~196 K in the lower stratosphere (*25*). Arctic polar vortex conditions during winter 1994–95 were suitable for NAT occurrence on up to 50% of the vortex area, ensuring long lifetimes of NAT particles (Fig. 2A). The fraction of the vortex that can contain ice particles is much smaller (Fig. 2B), which suggests that the key role played by ice particles may not be sedimentary removal of HNO_3 directly, but rather the initiation of NAT particles that can persist much longer than ice and denitrify the vortex by more gradual large-scale gravitational settling. Number densities < 0.1 cm^{-3} of large hydrate particles have indeed been observed under synoptic-scale conditions (*26*) as well as downstream of mesoscale ice PSCs (*27*).

Particle sedimentation was simulated on the basis of a three-dimensional (3D) grid structure with a resolution of 2.5° × 2.5° × 100 m (altitude) and covering 30° to 90°N latitude and 14 to 32 km altitude. Daily meteorological data from the European Centre for Medium-Range Weather Forecasts (ECMWF) were interpolated onto the model grid, with maximum horizontal gradients of potential vorticity used to define the vortex edge. Volume mixing ratios of H_2O and HNO_3 were initialized using observed profiles (*28*). We assumed that $HNO_3 = NO_y$, typical for midwinter conditions in the polar vortex. Particle sedimentation rates, which are a function of particle radii, were calculated at each time step in each grid volume in terms of condensed H_2O and HNO_3 amounts and prescribed particle number densities (n_{ice}, n_{NAT}). Ice nucleated in a grid volume whenever $T \leq T_{ice} - \Delta T_{ice}$, where ΔT_{ice} is an effective supercooling. The amount of ice was determined assuming thermodynamic equilibrium, equally distributed among the particles, and then allowed to take up HNO_3. The NAT residuals released upon ice evaporation were also assumed to be in thermodynamic equilibrium. In addition, subsidence of air was taken into account by using time- and altitude-dependent descent rates (typically 20 to 170 m/day) retrieved from 1994–95 Halogen Occultation Experiment (HALOE) hydrogen fluoride measurements using the method of Müller *et al.* (*3*).

Although vertical transport was treated in detail, horizontal transport has been simplified in our model. First, the vortex was treated as completely isolated from mid-latitudes. This is a good assumption above ~17 km altitude (~420 K potential temperature) (*15, 29*), although latitudinal mixing below this altitude may lead to a weaker nitrification than predicted by the model. Second, we chose a statistical approach to simulate the horizontal motion: For each time step, particles were formed on the basis of the interpolated 3D ECMWF temperature field and displaced vertically according to their sedimentation velocities, and then their HNO_3 was homogeneously distributed over the entire vortex area on their new altitude level (which allows us to avoid using an involved 3D advection scheme). This simplification is justified because the characteristic time for denitrification of ~1 month (Fig. 2C) gives sufficient time for a reasonable amount of horizontal mixing. This is consistent with similar denitrification (*17*) and nitrification (*16*) features observed on 5 days, which suggests a nonlocalized phenomenon. The neglect of horizontal gradients in HNO_3 and H_2O affects the calculated T_{ice} and T_{NAT} negligibly (*30*). A more serious problem is that horizontal homogenization might lead to NAT or ice seeding of previously unaffected grid volumes. Although this process is desired in cases where grid volumes are within advective reach of the NAT source regions over Northern Europe and Siberia, unconnected volumes might become activated as well. However, in part this is parried by properly adjusting the effective supercooling, ΔT_{ice}, to 1.5 K, yielding excellent agreement of computed (red curve, Fig. 1A) and observed (■, Fig. 1A) values of NO_y on 11 February 1995. This clearly is a

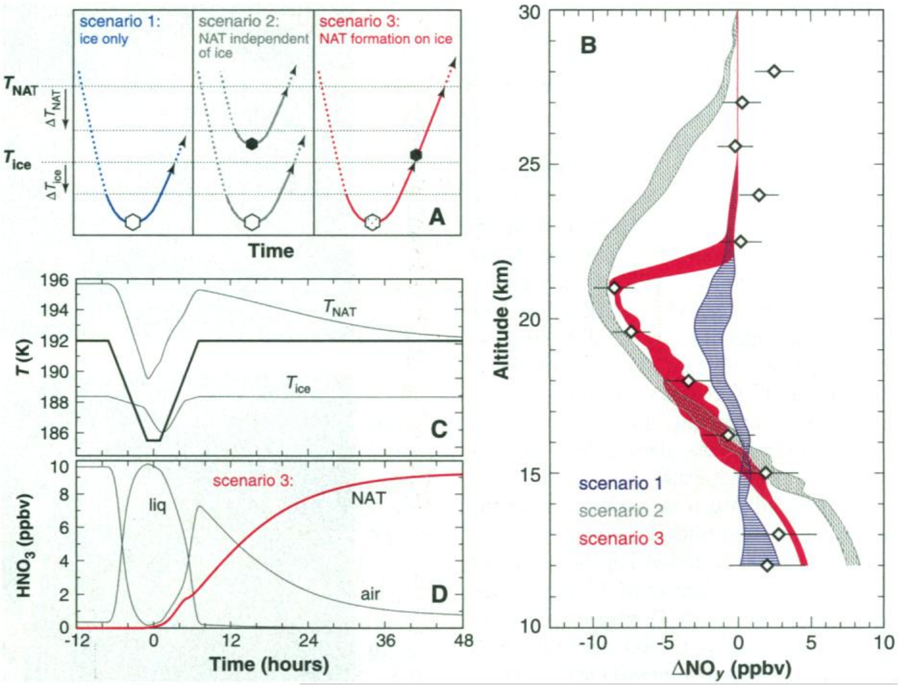

Fig. 3. (**A**) Different microphysical mechanisms used in the denitrification model: scenario 1, nucleation (at T_{ice} – 1.5 K) and sedimentation of ice particles only; scenario 2, assuming additional nucleation of NAT particles (at T_{NAT} – 2.5 K) independently of ice formation; scenario 3, assuming NAT particles to nucleate on ice particles and to be released upon warming above the frost point. (**B**) Vertical redistribution of NO_y as a result of scenarios 1 to 3 compared to MIPAS-B observations. Colored regions show ΔNO_y calculated using ECMWF temperatures unchanged and lowered by 1 K. Measured ΔNO_y is also shown (◇). (**C** and **D**) Temperature history and HNO_3 partitioning in scenario 3 along an idealized trajectory using a full kinetic treatment (*27*) of an aerosol distribution characteristic for the lower Arctic stratosphere.

weak point of this study that requires backup by advective 3D models, but analogy with the Antarctic suggests that this is unlikely to affect our prediction concerning denitrification in a future colder Arctic stratosphere.

The development of the NO_y profile was simulated on the basis of four scenarios with different microphysical assumptions (Fig. 3A). Scenario 0 (dashed line, Fig. 1A) considers exclusively the effect of subsiding vortex air on the vertical profile of NO_y and H_2O. The calculated NO_y, based on time- and altitude-dependent subsidence rates alone, shows excellent agreement with NO_y^* deduced from N_2O measurements on 11 February 1995 (□, Fig. 1A). For all other scenarios, the parameter set in best agreement with the observations is $n_{ice} = n_{NAT} = 5 \times 10^{-3}$ cm^{-3} and ΔT_{ice} =1.5 K (*31*). A simulation with ice particles alone (scenario 1, Fig. 3B) did not cause strong denitrification because the large particle radius ($r \approx 15$ μm) means that the ice particles sediment out in too restricted a region of the vortex (white contours, Fig. 2B). If in addition NAT particles are allowed to form 2.5 K below T_{NAT} (again with 5×10^{-3} particles per cubic centimeter) independently of ice (scenario 2), the model predicts strong denitrification. However, this extends well above the altitude at which ice can form and above the level of observed denitrification, and is therefore inconsistent with the characteristic altitude profile given by the measurements. However, if NAT is allowed to nucleate only on ice particles (scenario 3), as suggested by laboratory work (*32*), the model calculations are in striking agreement with the observations. Despite this coupling, the effect on the water vapor profile is small (Fig. 1B) because of the relatively short lifetime of ice particles under Arctic conditions. The formation of NAT on ice and the growth of NAT residuals by vapor deposition at the expense of ternary droplets [that is, a Bergeron-Findeisen process (*33*)] is shown in Fig. 3, C and D, revealing a characteristic time for their growth of ~1 day.

The results are highly sensitive to temperature changes (Fig. 4). Increasing the temperature by only 1 K essentially switches off denitrification, highlighting the strong requirement of ice formation to initiate the process. On the other hand, decreasing the temperature leads to a steady increase in the calculated denitrification. Sensitivity studies were performed for all scenarios by altering all model parameters (n_{ice}, n_{NAT}, ΔT_{ice}, ΔT_{NAT}) in every possible combination. These tests revealed that only scenario 3 was capable of reproducing the measurements, in particular the sharp shoulder in observed denitrification. Increases in n_{ice} and n_{NAT} by a factor of 4 or in ΔT_{ice} by 1 K can be compensated by a decrease in synoptic temperatures by 1 K, which is well within the temperature uncertainties (*31*). A change of 1 K would also compensate for incomplete uptake of HNO_3 due to kinetic constraints, say to only 80% of the thermodynamic value as in Fig. 3, C and D (*34*).

It has been suggested that denitrification might result if the lifetime of ice particles were prolonged as a result of NAT coating (*24*). The model in its present form is not suited to simulate this mechanism. However, the rapid sedimentation rates of such NAT-coated ice particles and the small regions over which ice can form means that they are likely to denitrify only a highly restricted portion of the polar vortex.

We have investigated the effect of denitrification on inorganic chlorine species partitioning and ozone depletion in a comprehensive photochemical box model [with liquid-phase microphysics and heterogeneous chemistry affecting $ClONO_2$, HCl, HOCl, and N_2O_5 (*35*)] by means of polar vortex-filling trajectories spanning the entire winter (Fig. 5). Two simulations were performed. First, diabatic subsidence of the air alone was considered. This leads to a constant NO_y mixing ratio in the descending air parcels, which is distributed between the various species in the NO_y family by chemical reactions in the model. In a second simulation, HNO_3 was reduced in line with that calculated in the sedimentation model, resulting in an HNO_3 mixing ratio of 6 ppbv at 19 km altitude on 15 February 1995 (at the level of maximum denitrification). This permanent loss of HNO_3 was then assumed to persist in the air parcels to the end of the simulation period on 15 April 1995 (*36*).

Figure 5 compares the ozone loss calculated by the model without and with denitrification for the winter 1994–95 (blue curves). By the end of the model period on 15 April the difference in ozone is more than 0.6 ppmv. This is equivalent to 55% more local ozone loss in the air parcels with denitrification than without. This considerable additional ozone loss occurs at an altitude corresponding to the approximate center of the ozone layer, hence the effect on the total ozone column is likely to be substantial (*8*).

A comparison with experimentally de-

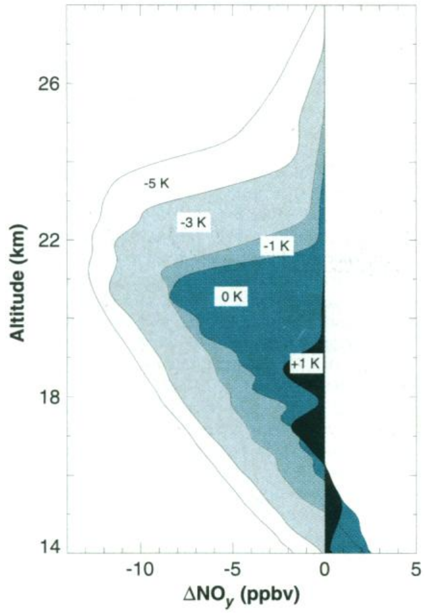

Fig. 4. Sensitivity of the simulated denitrification profile to systematic shifts in the synoptic temperatures, assuming scenario 3.

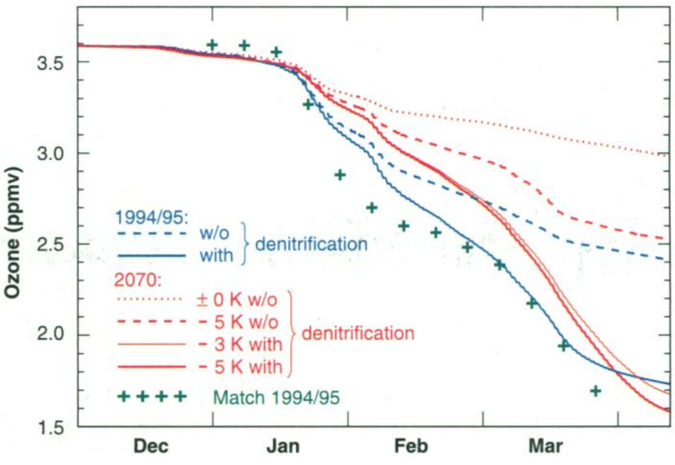

Fig. 5. Effect of denitrification on ozone depletion in a chemical box model. The results shown refer to an average of 190 trajectories initially distributed evenly (in the *x-y* direction) throughout the polar vortex. Blue curves refer to winter 1994–95 and are compared to measured ozone losses (green crosses) derived from the 1994–95 Match campaign (*4*) for the average potential temperature of the 190 trajectories as they descend. The simulation was performed from 1 December 1994 to 15 April 1995, starting at 550 K. Air parcels were advected using ECMWF analyzed winds, including diabatic descent derived from a radiative transfer model. On 31 March 1995 the potential temperatures of the trajectories are between 455 and 463 K with an average of 459 K. Simulations were performed to coincide with the maximum in denitrification, with the trajectories at 19 km altitude on 15 February 1995. The standard deviation about the average ozone value was at most ±15%. Red curves are future scenarios assuming a 45% decrease in total inorganic chlorine (*2*) and various assumed greenhouse gas–induced temperature decreases of the stratosphere.

rived chemical ozone loss from the 1994–95 Match campaign (*4*) indicates good agreement with our model results only if denitrification is included (besides a deviation in January, which cannot be explained in terms of denitrification). Temperatures would have to be considerably lower than they really were in March–April 1995 if continuous heterogeneous chlorine activation and denoxification alone were to be responsible for the observed ozone loss.

Global climate model simulations indicate that the stratospheric temperatures in the future are likely to be lower than those of recent years (*9, 10*). We have simulated a future scenario in which the overall Arctic vortex temperature was reduced by 5 K, which is predicted to occur in the Arctic lower stratosphere around the year 2070 in a 2 × CO_2 climate (*9*). Then the denitrification model simulation (Fig. 4) indicates sedimentary removal of more than 80% of the available NO_y over a wide altitude range. To test the effect of this on ozone depletion, we performed a chemical model simulation with temperatures reduced by 5 K relative to winter 1994–95 and a total inorganic chlorine mixing ratio of 1.75 ppbv, 45% lower than in our simulations of winter 1994–95 (*2*), as expected in 2070. Such a stratospheric chlorine loading is similar to concentrations around the year 1980. Neglecting denitrification, the combined effect of lower chlorine concentrations and lower temperatures is to slightly reduce the total ozone loss on the level we investigated (compare dashed curves in Fig. 5). Hence, the lower chlorine concentrations are largely offset by the more frequent PSC-induced chlorine activation. In stark contrast, including the effect of denitrification (solid red curve, Fig. 5) leads to as much as 0.9 ppmv more ozone loss, and hence a lower final ozone mixing ratio than predicted for winter 1994–95.

To test the dependence of the sedimentation microphysics and chemistry on the magnitude of future stratospheric cooling, we repeated the calculation assuming temperatures 3 K lower than in winter 1994–95. The magnitude of denitrification is not substantially reduced over a wide altitude range (Fig. 4). The resulting ozone loss (thin red curve, Fig. 5) is marginally lower than the case with temperatures 5 K lower, suggesting the results to be rather insensitive to the precise greenhouse scenario. Moreover, observations show increasing stratospheric water vapor (*37*), which—if the trend continues—will lead to further enhanced ice and NAT particle formation. A further sensitivity test assuming 50% more water vapor and temperatures 5 K lower than in 1994–95 led to greater denitrification and a final ozone mixing ratio of only 1.3 ppmv.

The relative importance of denitrification in determining ozone losses in a future colder stratosphere can be put into context by comparing with a reference case, in which the inorganic chlorine mixing ratio was reduced to expected 2070 levels (1.75 ppbv) but temperatures were left unchanged from winter 1994–95. This control case yielded a total ozone loss by the end of the winter of only 0.6 ppmv (dotted red curve, Fig. 5). In our model calculations, 5 K cooling alone leads to 0.45 ppmv more ozone loss (dashed red curve), whereas the associated denitrification increases this to 1.4 ppmv (solid red curve), thus enhancing cooling-induced ozone losses by more than a factor of 3. However, it should be noted that the meteorology of the Arctic vortex is variable and that the predictions here are made for a cold winter with a stable vortex.

In a future climate with a colder stratosphere and lower amounts of inorganic chlorine, Antarctic ozone depletion is likely to decline somewhat in response to lower chlorine concentrations. In contrast to the Arctic, this reduced ozone loss will not be compensated by increasing denitrification, which is already close to complete in the Antarctic. It therefore becomes possible that ozone losses over both poles will be very similar, in stark contrast to the situation today.

References and Notes

1. S. A. Montzka *et al.*, *Science* **272**, 1318 (1996).
2. S. Solomon and D. J. Wuebbels, in *Scientific Assessment of Ozone Depletion: 1994* (Report no. 37, WMO, Geneva, Switzerland, 1995), chap. 13.
3. R. Müller *et al.*, *J. Geophys. Res.* **101**, 12531 (1996).
4. M. Rex *et al.*, *J. Atmos. Chem.* **32**, 35 (1999).
5. B. Naujokat and S. Pawson, *Geophys. Res. Lett.* **23**, 3703 (1996); R. W. Zurek *et al.*, *ibid.*, p. 289; L. Coy *et al.*, *ibid.* **24**, 2693 (1997).
6. S. Solomon, *Nature* **347**, 347 (1990); D. W. Fahey *et al.*, *ibid.* **344**, 321 (1990); R. J. Salawitch *et al.*, *Science* **261**, 1146 (1993).
7. R. W. Portmann *et al.*, *J. Geophys. Res.* **101**, 22991 (1996).
8. M. P. Chipperfield and J. A. Pyle, *ibid.* **103**, 28389 (1998).
9. D. T. Shindell *et al.*, *Nature* **392**, 598 (1998).
10. J. Austin *et al.*, *ibid.* **360**, 221 (1992); G. Pitari and L. Ricciardulli, *Geophys. Res. Lett.* **21**, 1791 (1994); M. Dameris *et al.*, *ibid.* **25**, 3579 (1998); H.-F. Graf *et al.*, *J. Geophys. Res.* **103**, 11251 (1998).
11. J. F. Mahfouf *et al.*, *Clim. Dyn.* **9**, 345 (1994).
12. MIPAS-B (Michelson Interferometer for Passive Atmospheric Sounding) is a cryogenic balloon-borne limb emission sounder based on the Fourier transform infrared spectroscopy technique. A first version of this instrument was developed and flown in the late 1980s and early 1990s [H. Fischer and H. Oelhaf, *Appl. Opt.* **35**, 2787 (1996)]. The data reported here were obtained with the advanced second version (MIPAS-B2) during its first flight. MIPAS-B2 allows observations of all NO_y components and N_2O. The total reactive gaseous nitrogen obtained from MIPAS-B has 1σ uncertainties between 0.5 and 1 ppbv within the altitude range of 13 to 28 km with an altitude resolution of 2 to 3 km. For details see T. von Clarmann *et al.*, *J. Geophys. Res.* **102**, 16157 (1997); G. Wetzel *et al.*, *ibid.*, p. 19177.
13. NO_y^* was derived from MIPAS-N_2O using correlations from C. P. Rinsland *et al.* [*Geophys. Res. Lett.* **23**, 2397 (1996)] for N_2O < 120 ppbv, and from M. Loewenstein *et al.* [*ibid.* **20**, 2531 (1993)] for N_2O > 120 ppbv.
14. H. A. Michelsen *et al.*, *J. Geophys. Res.* **103**, 28347 (1998).
15. Michelsen *et al.* (*14*) demonstrated that the nonlinear relation between CH_4 and N_2O from ATMOS measurements can be used to infer the amount of mixing between in-vortex and out-of-vortex air. This quantified mixing effect may then be subtracted from the total NO_y deficit derived from the nonlinear NO_y/N_2O relation, leading to at most 18% being due to mixing. However, the same analysis based on MIPAS CH_4/N_2O reference profiles obtained from mid-latitude measurements (instead of ATMOS) shows a mixing effect of less than 5% due to a smaller nonlinearity, which is consistent with the cryo/grab-sampler reference data by A. Engel *et al.* [*J. Geophys. Res.* **101**, 14495 (1996)].
16. H. Fischer *et al.*, *J. Geophys. Res.* **102**, 23559 (1997).
17. T. Sugita *et al.*, *ibid.* **103**, 16221 (1998).
18. F. Arnold *et al.*, *Nature* **342**, 493 (1989); G. Huebler *et al.*, *Geophys. Res. Lett.* **17**, 453 (1990); E. J. Hintsa *et al.*, *ibid.* **25**, 501 (1998); F. Arnold *et al.*, *J. Atmos. Chem.* **30**, 49 (1998).
19. K. S. Carslaw *et al.*, *Rev. Geophys.* **35**, 125 (1997).
20. The terminal velocity $v(r)$ of a small particle in air depends mainly on its radius r but also on the density ρ and viscosity η of the surrounding air. Depending on the resulting Reynolds number, different regimes are considered (Cunningham, Stokes, and Best regimes) [R. Müller and Th. Peter, *Ber. Bunsenges. Phys. Chem.* **96**, 353 (1992)]. Typical velocities under stratospheric conditions are $v(1\ \mu m) \approx 1$ m/hour, $v(5\ \mu m) \approx 20$ m/hour, $v(10\ \mu m) \approx 60$ m/hour.
21. O. B. Toon *et al.*, *Geophys. Res. Lett.* **17**, 445 (1990).
22. U.-M. Biermann *et al.*, *ibid.* **25**, 3939 (1998).
23. J. E. Dye *et al.*, *J. Geophys. Res.* **97**, 8015 (1992).
24. S. C. Wofsy *et al.*, *Geophys. Res. Lett.* **17**, 449 (1990); Th. Peter *et al.*, *ibid.* **21**, 1331 (1994).
25. D. R. Hanson and K. Mauersberger, *ibid.* **15**, 855 (1988).
26. Th. Peter, *Annu. Rev. Phys. Chem.* **48**, 785 (1997).
27. K. S. Carslaw *et al.*, *J. Geophys. Res.* **103**, 5785 (1998).
28. Water vapor mixing ratios were initialized using HALOE measurements inside the polar vortex between 12 and 40 km on 5 December 1994. NO_y was initialized from a mid-latitude profile (12 to 34 km) on 12 October 1994 [V. Kondo *et al.*, *Geophys. Res. Lett.* **23**, 2369 (1996)].
29. G. L. Manney *et al.*, *J. Atmos. Sci.* **51**, 2973 (1994).
30. Even a halving or doubling of HNO_3 or a 20% change in H_2O causes changes in T_{ice} and T_{NAT} on the order of ~1 K (*25*) and therefore much smaller than the uncertainty of the temperature data themselves (*31*).
31. The assumed supercooling requirement is probably a lower limit, and reflects the fact that ice may in reality also be formed in mesoscale cooling events. There is also evidence that ECMWF temperatures might have a warm bias of at least 1 to 2 K [B. M. Knudsen, *Geophys. Res. Lett.* **23**, 3747 (1996)].
32. See T. Koop *et al.*, *Geophys. Res. Lett.* **22**, 917 (1995). There are possibly other pathways leading to NAT nucleation without preceding ice formation, but they are either still speculative (for example, heterogeneous nucleation on nuclei of unknown composition or NAT formation from amorphous nonliquid HNO_3/H_2O compounds) or the necessary temperatures differ only slightly from T_{ice} (for example, NAT formation induced by sulfuric acid tetrahydrate deliquescence). Ice-independent pathways for NAT nucleation are treated in scenario 2 and yield less good agreement with the observed NO_y redistribution.
33. H. R. Pruppacher and J. D. Klett, *Microphysics of Clouds and Precipitation* (Kluwer Academic, Dordrecht, Netherlands, ed. 2, 1997), pp. 546–550.
34. The model uses a 24-hour time step. In another sensitivity test we also considered the kinetics of the uptake and growth processes, but found no strong dependence: The shortening of the model time step to 6 hours was largely balanced by introducing simplified diffusion uptake kinetics.
35. K. S. Carslaw *et al.*, *Geophys. Res. Lett.* **24**, 1747 (1997).
36. Concerning the effect of mixing in late winter, we compared the MIPAS CH_4 vertical profile on 11 February 1995 with HALOE satellite data for March and April 1995 [plate 5 of (*3*)] and found good agreement. The compactness of the profiles suggests a very stable vortex. At the same time these

profiles differ considerably from the out-of-vortex profiles, suggesting no or very little mixing until mid-April. That the vortex remains intact is also indicated by our diabatic trajectory calculation, and is in line with the meteorological analysis of Naujokat and co-workers (5) [*Polar Stratospheric Ozone, Proceedings of the Third European Workshop*, J. A. Pyle, N. R. P. Harris, G. T. Amanatidis, Eds. (European Communities, Luxembourg, 1996), p. 9] showing that the vortex remained stable until late March followed by a slow transition to summertime conditions in April, but with a circulation reversal not accomplished before the end of the month.

37. S. J. Oltmans and D. J. Hofmann, *Nature* **374**, 146 (1995).
38. We thank L. Froidevaux, H. Graf, P. Newman, W. Randel, S. Solomon, and three anonymous reviewers for very helpful discussions, R. van Dorland for a calculation of stratospheric cooling rates, and M. Rex and P. von der Gathen for providing the Match results before publication. In part, this work was funded by the German Ministry of Education and Research (BMBF) under contract 01 LO 9221/4 (POLECAT) and 01 LO 9401 (MIPAS-B) and by the European Union under contract ENVCT95-0050 (TOPOZ), EV5VCT93-0331 (SESAME), and ENVCT95-0155 (STREAM).

30 November 1998; accepted 15 February 1999

Decay of the GRB 990123 Optical Afterglow: Implications for the Fireball Model

Alberto J. Castro-Tirado,[1,5]* María Rosa Zapatero-Osorio,[2] Nicola Caon,[2] Luz Marina Cairós,[2] Jens Hjorth,[3] Holger Pedersen,[3] Michael I. Andersen,[4] Javier Gorosabel,[5] Corrado Bartolini,[6] Adriano Guarnieri,[6] Adalberto Piccioni,[6] Filippo Frontera,[7,8] Nicola Masetti,[8] Eliana Palazzi,[8] Elena Pian,[8] Jochen Greiner,[9] Renè Hudec,[10] Ram Sagar,[11] Anil K. Pandey,[11] Vinay Mohan,[11] Ramakant K. S. Yadav,[11] Nilakshi,[11] Gunnlaugur Björnsson,[12] Páll Jakobsson,[12] Ingunn Burud,[13] Frederic Courbin,[13] Gaetano Valentini,[14] Anna Piersimoni,[14] Jesús Aceituno,[15] Luz María Montoya,[15] Santos Pedraz,[15] Roland Gredel,[15] Charles F. Claver,[16] Travis A. Rector,[16] James E. Rhoads,[16] Fabian Walter,[17] Jürgen Ott,[18] Hans Hippelein,[19] Victor Sánchez-Béjar,[2] Carlos Gutiérrez,[2] Alejandro Oscoz,[2] Jin Zhu,[20] Jiansheng Chen,[20] Haotong Zhang,[20] Jianyan Wei,[20] Aiying Zhou,[20] Sergei Guziy,[21] Aleksei Shlyapnikov,[22] John Heise,[23] Enrico Costa,[24] Marco Feroci,[24] Luigi Piro[24]

Broad-band (ultraviolet to near-infrared) observations of the intense gamma ray burst GRB 990123 started ~8.5 hours after the event and continued until 18 February 1999. When combined with other data, in particular from the Robotic Telescope and Transient Source Experiment (ROTSE) and the Hubble Space Telescope (HST), evidence emerges for a smoothly declining light curve, suggesting some color dependence that could be related to a cooling break passing the ultraviolet-optical band at about 1 day after the high-energy event. The steeper decline rate seen after 1.5 to 2 days may be evidence for a collimated jet pointing toward the observer.

Gamma-ray bursts (GRBs) are brief flashes of cosmic high energy (~10 keV–10 GeV) photons. They have remained without any satisfactory explanation since their discovery in 1967 (*1*). With the advent of the Italian-Dutch x-ray satellite BeppoSAX, it is possible to conduct deep counterpart searches only a few hours after a burst. This led to the first detection of x-ray and optical afterglows for GRB 970228 (*2*). Subsequent observations have shown that about half of the well-localized GRBs can be associated with optical emission, that gradually fades away, over weeks to months (*3*). About 10 such cases are known. Models proposed before the first detection of optical afterglow (*4*) have been successful in describing the decline of the optical emission. The afterglow is modeled as due to synchrotron radiation from relativistically expanding matter, that collides with the interstellar medium.

GRB 990123 was detected at 09:47 universal time (UT) on 23 January 1999 by the GRB monitor (GRBM) and the wide-field camera (WFC) of BeppoSAX, and by three instruments on board the Compton Gamma-ray Observatory, the Burst and Transient Source Experiment (BATSE), the Compton Telescope (COMPTEL), and the Oriented Scintillation Spectrometer Experiment (OSSE). A complex light curve was obtained, lasting ~100 s (*5*). The γ-ray fluence was $\sim 5.1 \times 10^{-7}$ J m^{-2} (*6*). This places the burst in the top 0.3 % of the BATSE GRB fluence distribution and it is one of the brightest events within the COMPTEL and OSSE range (>0.7 MeV) (*7*).

After 6.0 hours, BeppoSAX was reoriented toward the burst location and a previously unknown x-ray source was detected (*8*). The source intensity, $1.6\ (\pm 0.2) \times 10^{-14}$ J m^{-2} s^{-1} (2 to 10 keV), makes this x-ray afterglow the brightest detected so far. Optical observation conducted in response to the location of the x-ray afterglow as determined by BeppoSAX led to the identification of an optical transient, the GRB optical afterglow (hereafter OA) (*9*), associated with the GRB. This OA was initially seen as an object of a red broad-band magnitude $R = 18.2$ (*10*). Optical observations had, however, begun much earlier. In response to the internet-transmitted trigger from BATSE, ROTSE at Los Alamos National Laboratories (*11*) had started wide-angle imaging 22 s after the beginning of the GRB. Off-line analysis, conducted after the above-mentioned identification, revealed that the OA had been detected already in the first exposure, and had peaked at visual broad-band magnitude $V \sim 9$, some seconds later.

Optical spectroscopic observations revealed that the redshift of the burst source is

---

[1] Instituto de Astrofísica de Andalucía, IAA-CSIC, Granada, Spain. [2] Instituto de Astrofísica de Canarias, La Laguna, Tenerife, Spain. [3] Astronomical Observatory, University of Copenhagen, Copenhagen, Denmark. [4] Nordic Optical Telescope, La Palma, Tenerife, Spain. [5] Laboratorio de Astrofísica Espacial y Física Fundamental, INTA, Madrid, Spain. [6] Dipartimento di Astronomia, Università di Bologna, Bologna, Italy. [7] Dipartimento di Fisica, Università di Ferrara, Ferrara, Italy. [8] Istituto Tecnologie e Studio Radiazioni Extraterrestri, CNR, Bologna, Italy. [9] Astrophysikalisches Institut, Potsdam, Germany. [10] Astronomical Institute, CZ-251 65 Ondrejov, Czech Republic. [11] U. P. State Observatory, Manora Park, Naini Tal, 263 129 India. [12] Science Institute, University of Iceland, Reykjavik, Iceland. [13] Institut d'Astrophysique et de Géophysique de Liège, Université de Liège, 4000 Liege, Belgium. [14] Osservatorio Astronomico "V. Cerulli," Teramo, Italy. [15] Calar Alto Observatory, Almería, Spain. [16] Kitt Peak National Observatory, Tucson AZ, 85726, USA. [17] Astronomical Observatory, University of Bonn, Germany. [18] Radioastronomisches Institut, 53121 Bonn, Germany. [19] Max-Plank Institut für Astronomie, Heidelberg, Germany. [20] Beijing Astronomical Observatory, Chinese Academy of Sciences, Beijing 100080, and Beijing Astrophysics Center, Beijing 100871, China. [21] Nikolaev University Observatory, Nikolskaya, 24, 327030 Nikolaev, Ukraine. [22] Nikolaev Space Research Group, Nikolaev Astronomical Observatory, 327030 Nikolaev, Ukraine. [23] Space Research Organization Netherlands, Utrecht, The Netherlands. [24] Istituto di Astrofisica Spaziale, CNR, Frascati, Italy.

*To whom correspondence should be addressed E-mail: ajct@laeff.esa.es